Tuning optical properties in random arrays of plasmon resonant nanoparticles

by

Stefan Schelm

A thesis submitted in fulfilment
of the requirements for the degree of
Doctor of Philosophy

Department of Applied Physics
Faculty of Science
University of Technology, Sydney
Sydney Australia

2005

CERTIFICATE OF ORIGINALITY

I certify that the work in this thesis has not previously been submitted for a degree nor has it been submitted as part of requirements for a degree except as fully acknowledged within the text. I also certify that the thesis has been written by me. Any help that I have received in my research work and the preparation of the thesis itself has been acknowledged. In addition, I certify that all information sources and literature used are indicated in the thesis.

Signature of Candidate

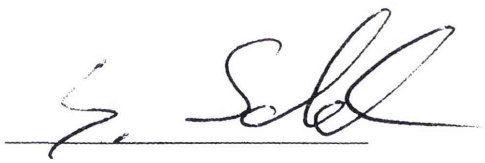

Acknowledgements

I would like to acknowledge the help of and thank the following persons and institutions for their help and support:

My supervisors Geoff. B. Smith and Matthew R. Phillips, the Microstructural Analysis Unit staff, especially Mark Berkhan and Richard Wuhrer, the people at the Department of Physics, chiefly Nicholas Armstrong, Annette Dowd and Abbas I. Maaroof for fruitful discussions, Geoff McCredie for practical and Linda Foley for administrative help. Furthermore, I have to thank Abbas I. Maaroof particularly for his large contribution to the chapter 6.

For their cooperation and use of their samples I'd like to thank the Commonwealth Scientific and Industrial Research Organisation (CSIRO) in Lindfield, Sydney, especially Gang Wei and the CSIRO in Melbourne.

For interesting discussions, their help and use of their SNOM I would like to thank the Surface Physics Group at Newcastle University, especially Chris McNeill, Daniel Cotton and Paul Dastoor. With regard to SNOM I'd also like to thank Alexandre Bouhelier and Jan Seidel for indulging my questions and helping me to improve my knowledge about SNOM.

I would also like to thank Juan Sotelo and Jacob Jonsson for interesting discussions and help during their stay and J. Prikulis and M. Käll for letting me use some of their results of random holes in gold films.

Furthermore, I am thankful for suggestions, by the referees, for the improvement of the quality and readability of the thesis.

Last but not least, I am grateful for the financial support by the BASF AG, Germany and the help of my family.

Preface

Parts of this thesis have been published in the following papers and proceedings:

- S. Schelm and G.B. Smith "Self-assembled gold nanoparticles with organic linkers", invited chapter to be published in Nanotechnology in Biology and Medicine (CRC Press, FL, to be published in 2006)
- S. Schelm, G. B. Smith, P. D. Garrett, W. K. Fisher "Tuning the surface plasmon resonance in nanoparticles for glazing applications", Journal of Applied Physics **97** (12), 124314 (2005)
- S. Schelm and G.B. Smith "Evaluation of the limits to the resonance tunability in metallic nano-shells with a spectral averaging method", Journal of the Optical Society of America A **22** (7), 1288 (2005)
- S. Schelm and G.B. Smith "Internal Electric Field Densities of Metal Nanoshells", Journal of Physical Chemistry B **109** (5), 1689 - 1694 (2005)
- G.B. Smith, A. Maaroof, R. Allan, S. Schelm, M. Cortie, G. Anstis "Optical response of nanostructured metal/dielectric composites and multilayers" (invited paper), Proceedings of SPIE Vol.5508 (Conference 5508: Complex Mediums V: Light and Complexity, 2004)
- S. Schelm and G.B. Smith "Field profiles for spherical conductive nanoparticles and metallic-shell/dielectric-core nanocomposites", Proceeding of SPIE Vol.5509 (Conference 5509: Nanomodeling, 2004)

- S. Schelm, G.B. Smith, G. Wei, A. Vella, L. Wieczorek, K.-H. Müller, B. Raguse "Double effective medium model for the optical properties of self-assembled gold nanoparticle films cross-linked with alkane dithiols", Nano Letters **4** (2), 335-339 (2004)

- S. Schelm, G.B. Smith, G. Wei, A. Vella, L. Wieczorek, K.-H. Müller, B. Raguse "Optical properties of dense self-assembled gold nanoparticle layers with organic linker molecules", Proceedings of SPIE Vol.5221 (Conference 5221: Plasmonics, 2003)

- S. Schelm and G.B. Smith "Dilute LaB6 nanoparticles in polymer as optimized clear solar control glazing", Applied Physics Letters **82** (24), 4346-4348 (2003)

Abstract

Small conductive particles show a resonant behaviour at wavelengths where bulk or thin film samples have no features. This resonance is caused by the collective oscillation of the free electrons in the particle and is called localised surface plasmon resonance. It is influenced by the shape of the particle, the surrounding medium and particle interaction.

I studied shape, matrix and interaction effects of metallic and metal-like particles in various systems with the aim to rationally tune the resonance to specific wavelengths for different applications.

Dilute samples of small LaB_6 particles were studied with regard to their NIR blocking performance. My analysis showed that they are more efficient than the alternative materials ITO and ATO. This is mainly due to the position of the LaB_6 particle resonance, which lies precisely in the spectral region which needs to be blocked (around 1 μm). I was able to model the optical properties of the window samples, using a dilute quasi-static approach for anisotropic particles.

Different embedding matrices and particle interaction have also an influence on the localised surface plasmon resonance. An example for a combination of matrix and interaction effects is a self-assembled gold particle film with organic linkers. Structural effects were especially important in these films, as was verified by electron microscopy. The optical properties were successfully modeled, using a two level effective medium approximation.

A different way to tune the resonance is to change the shell thickness to core size ratio in metallic nanoshells. The resulting spectral shift, though, is limited by

experimental realities for the metal coating and the onset of scattering for larger particles. The shell has two resonances, of which the low energy one can be tuned by the ratio mentioned above. This resonance also shows a different electric field profile to the normal dipole (and high energy shell) resonance. The field pattern also highlights a strong field gradient across the external shell interface and along the incident polarisation direction. The properties were calculated using Mie theory and the quasi-static approximation.

Finally, the far and near-field optical properties of thin silver films with randomly distributed holes were studied. They showed an enhanced absorption, due to coupling of the incident light into surface plasmon polaritons by the holes. Whereas the films did not show the enhanced transmission, which occurs in regular hole arrays, they still might provide some insight in the processes involved by helping to exclude some possible explanations.

Contents

Abstract vi

Glossary xix

1 Introduction 1

2 Techniques 4

2.1 Synthesis of Nanoparticles 4

2.1.1 Physical Routes 4

2.1.2 Chemical Routes 6

2.2 Experimental Characterisation Methods 7

2.2.1 Spectrophotometry 8

2.2.2 Ellipsometry 8

2.2.3 Scanning electron microscopy 9

2.2.4 Scanning Near-field Optical Microscopy 9

2.2.5 Other experimental techniques 12

2.3 Theoretical Methods 12

2.3.1 The Surface Plasmon, Size and Shape Effects 13

2.3.2 Mie Theory and Generalised Mie Theory 17

2.3.3 The quasi-static or Rayleigh limit 18

2.3.4 Effective Medium Approximations 21

2.3.5 Other Techniques 25

3 LaB_6 particles as NIR absorbers **27**

3.1 Introduction 27

3.2 Transparent Oxides 31

3.3 Synthesis of the LaB_6 nanoparticles 35

3.4 Characterisation 35

3.5 Modelling of the optical properties 39

3.6 NIR and Solar Performance 41

3.7 Scattering and Haze 44

3.8 Conclusion 49

4 Self-assembled gold NP films **51**

4.1 Introduction 51

4.2 Synthesis 55

4.3 Structural characterisation 57

4.4 Optical characterisation 62

4.5 SNOM 65

4.6 Double EMA model for the optical properties 75

4.7 Conclusion 83

5 Properties of metallic nanoshells **86**

5.1 Introduction 86

5.2 Resonance tuning and its limits 88

5.2.1 Theory 89

5.2.2 Results and Discussion 91

5.2.3 Conclusion 96

5.3 Field intensity profiles 97

5.3.1 Results and Discussion 98

5.3.2 Conclusion 110

5.4 Summary 112

6 Silver films with sub-wavelength holes **114**

6.1 Introduction 114

6.2 Sample preparation 115

6.3 Structural characterisation 115

6.4 Far-field characterisation 117

6.5 Near-field characterisation 121

6.6 Conclusion 130

7 Summary and Outlook **132**

Bibliography **138**

List of Figures

2.1 Size effect of equation 2.5 on the gold dielectric data of Ref. [1] for different effective radii $R_{eff} = \frac{R}{A}$. 17

2.2 Geometry of the quasi-static problem for a coated sphere. 19

3.1 Spectral density of the sun after passing through 1.5 times the air mass (solid line) and the photopic response of the human eye in the green (dashed line), where its sensitivity is highest. 30

3.2 Calculated absorption coefficient of ITO (solid line) and ATO (dashed line) in a medium with $n = 1.5$, based on the quasi-static sphere model with a volume fraction of 0.3%. 32

3.3 Calculated spectral transmittance of an undoped and ITO doped PVB laminated window, using the same clear glass sheets as in Fig. 3.8 33

3.4 Mie theory calculation of extinction efficiency of a ZnO:Al sphere with $R = 50$ nm and $n_{medium} = 1.5$. The optical data are taken from Ref. [2] for an Al content of 2.14 atomic%. 34

3.5 Transmittance of ZnO and Zno:Al particles in a polymer film on a quartz glass slide. The films have a particle concentration of 20 weight% and the Al content of prep 2 is larger than that of prep 1. The inset shows the region where the SPR is expected in more detail (see also figure 3.4). 34

3.6 Example TEM images of a PVB sheet, doped with 0.015 weight% of LaB_6 nanoparticles (contamination ZrO_2 particles are also visible). . . 36

3.7 High resolution SEM image of the Lab_6-ZrO_2 nanoparticle powder mix, as dried from solution. 37

3.8 Spectral transmittance of the full set of LaB_6 doped PVB laminated windows, including one window with undoped PVB. The insert shows the sandwich structure of the samples, consisting of the doped PVB sheet between two clear glass sheets. 38

3.9 Measured and modeled absorption coefficient as a function of LaB_6 concentration in PVB. Modelling is for two perpendicular incident polarisations using tow different depolarisation factors in a spheroid. . 38

3.10 Theoretical scattering efficiency of spherical LaB_6 nanoparticles embedded in a polymer with refractive index $n = 1.47$ for sizes ranging from 50 nm to 200 nm diameters. The inset shows the ratio of scattering to absorption efficiency at 500 nm as a function of the sphere radius to highlight the increasing influence of scattering for larger spheres in the visible. 46

3.11 4π corrected calculated backscattering efficiency for the same LaB_6 spheres shown in figure 3.10, $n_{medium} = 1.47$. 47

4.1 Two different schemes to prepare films of organically cross-linked gold nanoparticles. a) layer-by-layer (LBL) method, b) solution filtration method 56

4.2 SEM images for a) the C8 cross-linker and b) the C15 cross-linker for films filtrated from 3 ml of solution. 59

4.3 SEM images for the C2 cross-linker filtrated from 7.5 ml of solution. . 60

4.4 SEM images: a) C8, b) C15 dithiol cross-linked gold nanoparticle film, filtrated from 0.5 ml of solution. The differences in contrast and detail between the images are due to the use of different detectors: a) standard secondary electron detector, b) in-lens secondary electron detector. 61

4.5 SEM of a cross-section of a film with the C15 linker and filtrated from 7.5 ml of solution through a porous alumina substrate. The dimension of the main image is 10x10 μm and for the inset 1x1 μm. . 62

4.6 Reflectance and transmittance for the C8 and C15 linker films filtrated from 4 ml of solution. 63

4.7 Effective $\langle n \rangle$ and $\langle k \rangle$ values for the continuous films created from volumes between 3 ml and 7.5 ml (see Table 4.1) for the three linker lengths studied. The experimental values were measured with ellipsometry and the theoretical values are from our double EMA model. The dielectric data for bulk gold is included for comparison (from Ref. [1], note the different scale for this panel). 64

4.8 SEM image of the thicker C15 linker film created from 7.5 ml of solution. It highlights the appearance of cracks and the compacting of the film, which in effect reduces the void phase (compare to figure 4.2). 66

4.9 AFM (top) and SNOM (bottom) images for a) the C8 cross-linker and b) the C15 cross-linker for films filtrated from 7.5 ml of solution (the gray scale of the SNOM images is not linear, in order to improve their contrast) 67

4.10 10x10 μm sized SNOM images for a) the C8 cross-linker and b) the C15 cross-linker for films filtrated from 7.5 ml of solution (linear gray scale). 68

4.11 PDF for the four presented SNOM images: a) the 5x5 μm C8 (Fig. 4.9 (a)), b) the 10x10 μm C8 (Fig. 4.10 (a)), c) the 5x5 μm C15(Fig. 4.9 (b)) and d) the 10x10 μm C15 (Fig. 4.10 (b)) image. 70

4.12 Illustration of the two different plasmon propagation concepts: a) LSP coupling and hopping propagation and b) SPP on a metal surface. . . 73

4.13 Schematic of possible double EMA models, showing the conceptual differences between a MG and BR effective medium. The model which seems to be the most appropriate in our case, is the building the final effective medium C. 77

4.14 Volume fraction dependence of f_{AuL} and f_{void} on the chain length of the linker molecule 80

4.15 Comparison between experimental ellipsometric dielectric data (solid line) and MG (dotted line) and BR (dashed line) EMA for a film in the low coverage regime (filtrated volume: 1 ml, see Table 1) 82

5.1 Schematic of the origin of the mean free path $R_{GH} = \frac{1}{2}\sqrt[3]{(r_{shell} - r_{core})\, q^2}$ in metallic shells on dielectric cores, as proposed by Granqvist and Hunderi [3]. 91

5.2 3D plot of the scattering contribution $\mathcal{S}_\Lambda$ for the studied gold-shell SiO_2-core particles in a medium with $n_{host} = 1.49$. The circles represent results for solid gold particles (shown with an arbitrary δ ratio of 1). 92

5.3 The scattering contribution $\mathcal{S}_\Lambda$ for $\Lambda = 300 - 2000$ nm as a function of the total radius of the particle for different δ ratios in a medium with $n_{host} = 1.49$. The solid line shows the result for the solid sphere. The dotted line shows $\mathcal{S}_\Lambda$ in the same range for homogeneous silver spheres. 93

5.4 Calculated extinction, scattering and absorption efficiencies for spherical gold-shells on a silica-core with δ=0.1 and $r_{total} = 110$ nm (solid) and $r_{total} = 55$ nm (dashed). $\mathcal{S}_\Lambda$ for both curves can be seen in Fig. 5.3. 94

5.5 Calculated extinction efficiency for the solid gold sphere and gold-shell on silica-core spherical particles for $r_{total} = 150$ nm and δ between 0.5 and 2 (solid curves, the curves are actually so close that they are indistinguishable). The dashed curve is for a core-shell particle with $r_{total} = 200$ nm and $\delta = 1$. 95

5.6 Extinction efficiency for a homogeneous sphere with $R = 18$ nm (solid line) and a gold shell on a core with $n_{core} = 1.33$, $R_{core} = 15$ nm and $R_{shell} = 18$ nm (dashed line), in a medium with $n_{medium} = 1.33$. The marks show the wavelengths for which the $|\mathbf{E}|^2/|E_0|^2$ plots in the other figures are calculated. The gold dielectric function is size corrected in both cases, as explained in the text. 100

5.7 $|\mathbf{E}|^2/|E_0|^2$ contour plots for two principal planes for a 3 nm thick gold shell (size corrected, see text) on a core with radius of 18 nm with $n_{core} = n_{medium} = 1.33$ at the resonance wavelength for this system of 708 nm. The colour scale is logarithmic. 101

5.8 The same images as in Fig. 5.7, but with a reduced scale to show the field gradient inside the core. 102

5.9 Contour plots of $|\mathbf{E}|^2/|E_0|^2$ for two principal planes and the same core-shell particle as in figure 5.7, but at the off-resonance wavelength of 1000 nm. Again the colour scale is logarithmic. 104

5.10 Same as Fig. 5.9 but with a reduced scale to show the structure in the core. 105

5.11 $|\mathbf{E}|^2/|E_0|^2$ contour plots for two principal planes for a homogeneous gold sphere with a radius of 18 nm (size corrected, see text) in a medium with $n_{medium} = 1.33$ at the resonance wavelength for this system of 532 nm. The colour scale is logarithmic (note also the reduced scale). 106

5.12 The same sphere as in Fig. 5.11, but at the off-resonance wavelength of 1000 nm. 107

5.13 $|\mathbf{E}|^2/|E_0|^2$ contour plots for the asymmetric (top row, at 328 nm) and symmetric (bottom row, at 526 nm) shell mode in a silver shell on a silica core with $R_{core} = 20$ nm, $R_{shell} = 25$ nm and $n_{medium} = 1.0$. The right column is the Mie calculation as used in the other images. The left column is a quasi-static calculation with the same geometrical factors, including the external field. The $\mathbf{k}$ vector is only of interest for the Mie results. 109

6.1 SEM images of the randomly structured silver films: a) low hole concentration, b) high hole concentration. The insets show larger magnifications of the same films. 116

6.2 10x10 μm AFM images of the structured silver films: a) low hole concentration, b) high hole concentration. 117

6.3 Reflectance and transmittance of an unstructured silver film (solid curve), as well as the low hole concentration (dashed curve) and high hole concentration (dotted curve) structured silver films. The thickness of all films is 80 nm. 118

6.4 Absorption of an unstructured silver film (solid curve), as well as the low hole concentration (dashed curve) and high hole concentration (dotted curve) structured silver films. The thickness of all films is 80 nm. 118

6.5 Visualisation of the different momenta involved in the coupling process. The correction for the angle of incidence is also shown. 120

6.6 10x10 μm AFM (left) and SNOM (right) images of the high hole concentration sample. The bottom image is a composition of these two images, the height is from the AFM and the colour from the SNOM image. The composite image shows the "bottom" of the 3D graph to highlight the hole structures, which can be seen as peaks in this representation. The arrows act as a guide to the eye showing the starting point and direction of the scan. 123

6.7 10x10 μm AFM (left) and SNOM (right) images of the low hole concentration sample. 125

6.8 10x10 μm AFM (left) and SNOM (right) images of a flat section of the low hole concentration sample. 126

6.9 AFM (left) and SNOM (right) images of a gold film with a higher hole concentration than our samples (courtesy of J. Prikulis and M. Käll and reprinted in part with permission from Ref. [4]. Copyright 2004 American Chemical Society). 127

6.10 Probability density function (PDF) for the SNOM images of the structured metal films: a) high hole concentration sample, from Fig. 6.6, b) low hole concentration sample, from Fig. 6.7 (top row), c) flat region of the low concentration sample, from Fig. 6.8 and d) very high hole concentration gold sample, from Fig. 6.9 (courtesy of J. Prikulis and M. Käll). 128

List of Tables

3.1 Comparison between the actual concentration values and the values gained from the model of the nanoparticle doped PVB sheet. 41

3.2 Visible and solar transmittance (T_{vis}, T_{sol}), $\frac{T_{vis}}{T_{sol}}$, SHGC, K^* and (x, y, z) colour coordinates for the window systems studied, containing different concentrations of LaB_6 and the ITO example shown in figure 3.3. 43

3.3 Relative forward scattering intensity $\mathcal{I}_{FS}$, as defined in Eq. 3.6, for isolated LaB_6 spheres at 350 nm (Rayleigh scattering) and 1000 nm (SPR scattering) 48

4.1 Film thicknesses based on extrapolation from cross-section analysis (asterisks denote actually measured cross-sections) 58

4.2 Volume fractions from the fit of the optical model to the ellipsometry data for the three different cross linkers 79

Glossary

AFM	Atomic Force Microscope
BR	Bruggeman EMA Scheme
CSIRO	Commonwealth Scientific and Industrial Research Organisation
DDA	Discrete Dipole Approximation
EMA	Effective Medium Approximation
LBL	Layer-by-Layer deposition
LSP	Localised Surface Plasmon
MG	Maxwell Garnett EMA Scheme
NP	Nanoparticle
NF	Near-field
PDF	Probability Density Function
SAM	Self-Assembled Monolayer
SEM	Scanning Electron Microscope
SERS	Surface Enhanced Raman Scattering
SHGC	Solar heat gain coefficient
SNOM	Scanning Near-Field Optical Microscope
SPP	Surface Plasmon Polariton
SPR	Surface Plasmon Resonance